Progress in Medical Devices
ISSN: 2957-5478

Zentime

Research Article https://doi.org/10.61189/143103ncllxn

Application and accuracy enhancement of an improved spatial registration method in electromagnetic navigation for tumor ablation surgery

Xinyao Li, Gaoshuai Chen, Xin Yang, Yuchao Liu, Yu Xia

The School of Mechanical Engineering, University of Shanghai for Science and Technology, Shanghai 200093, China.

Corresponding author: Xinyao Li.

Declaration of conflict of interest: None.

Received November 15, 2024; Accepted July 11, 2025; Published September 30, 2025

Highlights

- Proposed an improved SVD algorithm to reduce errors caused by electromagnetic interference, thereby enhancing the precision of surgical navigation systems.
- Validated the algorithm through puncture experiments on biomimetic tissue of angles 0°, 5°, and 10° , demonstrating high accuracy in simulating tumor localization.

Abstract

Objective: To enhance the accuracy and efficiency of tumor ablation procedures, this study integrated tumor ablation technology with a surgical navigation system and addressed errors induced by electromagnetic interference in clinical settings. **Methods:** An improved singular value decomposition (SVD) algorithm was proposed, which iteratively traversed the point set by selecting three corresponding points at a time to compute transformation matrices. Each matrix was applied to the original dataset, and the one yielding the minimum error between the transformed and target point sets was selected as the optimal solution. This approach mitigated the influence of individual outlier points and significantly reduced navigation errors caused by electromagnetic interference, thereby enhancing registration accuracy and robustness. **Results:** Experimental results demonstrated that the improved algorithm achieved high accuracy in simulating lesion localization. The root mean square error (RMSE) was employed as a quantitative metric. RMSE values were 0.85, 0.82, and 0.75 at rotation angles of 0°, 5°, and 10°, respectively, indicating minimal deviation between the transformed and target point clouds. **Conclusion:** Compared with the conventional SVD algorithm, the improved method yielded consistently lower RMSE values, confirming its effectiveness in minimizing electromagnetic navigation errors and enhancing registration accuracy.

Keywords: Tumor Ablation, surgical navigation system, electromagnetic interference and spatial registration

Introduction

With the global aging population, cancer treatment faces increasing new challenges and complexities. As a locoregional therapeutic approach, tumor ablation has gained widespread clinical adoption due to its minimally invasive nature, cost-effectiveness, and association with faster recovery. Recent developments have seen the integration of tumor ablation techniques with surgical navigation systems, forming a novel therapeutic paradigm in oncology. Surgical navigation systems reconstruct a three-dimensional spatial model based on preoperative imaging data to accurately localize tumors during surgery. These systems enable precise visualization of the tumor and surrounding critical structures. Surgeons can preoperatively plan the optimal surgical path using dedicated software and receive real-time feedback on instrument positioning throughout the procedure. This allows for effective avoidance of vital structures and accurate targeting of lesions for ablation or excision [1].

As these systems continue to evolve, they are

Address correspondence to: Xinyao Li, The School of Mechanical Engineering, University of Shanghai for Science and Technology, No. 516 Jungong Road, Yangpu District, Shanghai 200093, China. Tel: +86-15156575887; E-mail: 15156575887@163.com.

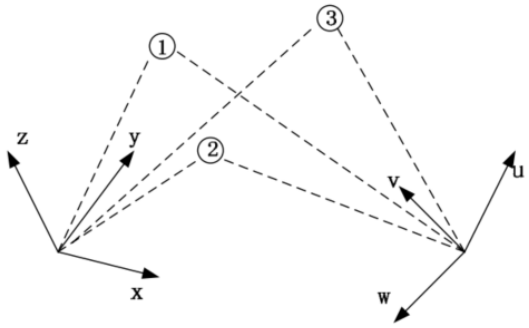

Figure 1. Schematic diagram of paired point-set registration.

increasingly used in minimally invasive procedures such as tumor thermal ablation, prostate surgery, and other laparoscopic interventions. Surgical navigation enhances anatomical clarity, optimizes intraoperative decision-making, and reduces the risk of complications. Several commercial optical navigation systems—such as the NDI Polaris, StealthStation, and Stryker ADAPT, are already in clinical use [2-4].

However, electromagnetic navigation systems remain susceptible to errors due to environmental interference [5]. These inaccuracies may lead to incomplete tumor ablation or unnecessary damage to healthy tissue, ultimately compromising therapeutic outcomes and increasing recurrence risk [6]. Clinical equipment and metallic instruments can reduce the accuracy and reliability of electromagnetic tracking systems, while limitations in real-time performance may further contribute to intraoperative errors [7, 8].

This study focuses on an improved spatial registration method based on electromagnetic navigation, which links magnetic field pose data with medical imaging to provide real-time visualization of the ablation needle's trajectory relative to the tumor. Specifically, we propose an enhanced singular value decomposition (SVD) algorithm to mitigate electromagnetic-induced errors and improve the precision and efficiency of the ablation procedure.

Surgical navigation systems are conceptually composed of two core components: medical imaging modalities and stereotactic positioning systems. The imaging module typically includes radiographic technologies such as X-ray, computed tomography, positron emission tomography, and magnetic resonance imaging. The positioning subsystem encompasses optical tracking, electromagnetic sensors, acoustic guidance, and articulated robotic arms. A critical function of these systems is spatial co-registration, which accurately aligns the patient's physical anatomy with virtual reconstructions derived from medical imaging, thereby enabling real-time visualization of surgical instruments relative to the target lesion during intervention procedures [9].

Despite advancements in medical imaging achieving submillimeter spatial resolution and stereotactic devices reaching micron-level positioning accuracy through sophisticated calibration protocols, the overall efficacy of surgical navigation platforms remains limited by deficiencies in spatial registration algorithms—particularly in multimodal image fusion and compensation for intraoperative tissue deformation. This technological bottleneck often results in registration errors exceeding 2–3 mm in clinical practice, significantly undermining the translation of theoretical precision into practical surgical accuracy.

To address registration inaccuracies, Zhou et al. employed a markerless registration method combined with spatial drift compensation techniques [10]. Li et al. applied the Coherent Point Drift algorithm based on Gaussian Mixture Models, to register abdominal point clouds in scenarios lacking prominent surface features [6]. Xiong et al. incorporated deformable self- and cross-attention mechanisms into point cloud registration, leveraging spatial local relational information as positional embeddings within a Spatial Deformable Transformer framework [11].

Currently, most surgical navigation systems rely on paired point-set registration, as illustrated in **Figure 1**. This method computes a spatial transformation that aligns two sets of points captured from different coordinate systems. It is favored for its stability, computational simplicity, and efficiency. Reference points are typically derived from external markers placed on the patient's skin or anatomical landmarks. These markers are localized in imaging data and linked to real-world coordinates through stereotactic calibration, thereby completing the co-registration between the patient's anatomy and the imaging dataset.

Paired point-set registration algorithms include the three-point method, quaternion-based approaches, and the SVD matrix decomposition method. Among them, the three-point method offers simplicity, rapid computation, and ease of implementation, requiring only three corresponding points to complete registration. However, its low accuracy and sensitivity to measurement errors limit its utility in high-pre-

cision contexts. Therefore, it is generally used for initial alignment rather than in scenarios requiring fine surgical navigation accuracy.

Materials and methods

SVD matrix factorization algorithm

In spatial transformation, the coordinates of corresponding reference points in different coordinate systems are often influenced by multiple factors and may not align precisely. Sources of error include device inaccuracies, stereotactic localization errors, and mechanical tolerances of surgical instruments. Therefore, the goal of spatial registration algorithms is to estimate the optimal transformation—specifically, the rotation matrix R and translation vector T—that minimizes the alignment error [12]. This optimization problem is defined as:

$$\mathrm{E(R,T)} = \sum_{i=1}^{m} \|q_i - (R^* p_i + T)\|^2 \quad (1)$$

In the equation, q_i represents the coordinates of the i-th control point in the target coordinate system; p_i denotes the coordinates of the i-th control point in the source coordinate system.

The transformation relationship is considered optimal, when $\mathrm{E(R,T)}$ is minimized. To reduce the impact of reference point errors, m (where m≥3) reference points are used to mitigate the influence of erroneous data on the overall result. Before solving the transformation relationship between the two-point sets, their centroids are first calculated as follows:

$$p_{\text{center}} = \frac{1}{\mathrm{m}} \sum_{i=1}^{\mathrm{m}} p_i \quad (i = 1,2,3 \ldots m) \quad (2)$$

$$q_{\text{center}} = \frac{1}{\mathrm{m}} \sum_{i=1}^{\mathrm{m}} q_i \quad (i = 1,2,3 \ldots m) \quad (3)$$

In the equation, p_{center} denotes the centroid of the control point set in the source coordinate system; q_{center} is the centroid in the target coordinate system.

Subsequently, the point sets are centered, as shown below.

$$p_i' = p_i - p_{\text{center}} \quad (4)$$

$$q_i' = q_i - q_{\text{center}} \quad (5)$$

where p'_i and q'_i are the centered coordinates of the i-th control point in the source and target coordinate system, respectively.

With this, Equation (1) simplifies to:

$$\mathrm{E(R,T)} = \sum_{i=1}^{\mathrm{m}} \|q_i' - \mathrm{R}p_i'\|^2 \quad (6)$$

From equation (6), minimizing $\mathrm{E(R,T)}$ reduces to determining the optimal rotation matrix R. To this end, the covariance matrix H is constructed:

$$\mathrm{H} = \sum_{i=1}^{\mathrm{m}} p_i' q_i'^{t} \quad (7)$$

SVD is performed on H:

$$\mathrm{H} = \mathrm{USV} \quad (8)$$

In the equation, both U and V are orthogonal matrices, and S is a diagonal matrix, with diagonal elements called singular values. This decomposition retains full covariance information and provides an important foundation for subsequent steps.

The matrix X is then defined as:

$$X = VU^t \quad (9)$$

The determinant of X is computed to detect potential inversion.

1) If $\det(\mathrm{X})>0$, then $\mathrm{R} = \mathrm{X}$.

2) If $\det(\mathrm{X})<0$, X is a reflection matrix (indicating inversion). In this case, V is adjusted:

If $\mathrm{V}=[\mathrm{v_1 v_2 v_3}]$, then let $\mathrm{V}'=[\mathrm{v_1 v_2 - v_3}]$. In this case:

$$\mathrm{X}' = \mathrm{V}'\mathrm{U}^{\mathrm{t}} \quad (10)$$

Thus, $\mathrm{R}=\mathrm{X}'$. In stereotactic navigation, however, mirror inversion does not occur; therefore, a detected $\det(\mathrm{X})<0$ suggests data inconsistencies that warrant further inspection.

Once R is obtained, the translation vector T is derived from the centroids:

$$\mathrm{T} = q_{\text{center}} - \mathrm{R}p_{\text{center}} \quad (11)$$

The R and T obtained via SVD thus represent the optimal solution, minimizing $\mathrm{E(R,T)}$.

SVD algorithm and registration improvement

SVD registration principle

To eliminate the influence of translational differences between point sets, the data should first be centered so that their centroids coincide with the origin. This preprocessing step allows the registration process to focus solely on the rotational relationship between the point sets, thereby avoiding biases introduced by translation [13].

Once the point sets are centered, the covariance matrix is computed. The covariance matrix captures the linear relationship between the two-point sets and quantifies the degree of correlation between corresponding elements [14]. It is defined as:

$$\sigma(p_i, q_i) = \frac{1}{n-1}\sum_{i=1}^{n} (p_i - \bar{p})(q_i - \bar{q}) \tag{12}$$

Where p_i and q_i represent the i-th observation points in the two-point sets, the covariance matrix Σ can be obtained as follows:

$$H = \begin{bmatrix} \omega(p_1, q_1) & \cdots & \omega(p_1, q_n) \\ \vdots & \ddots & \vdots \\ \omega(p_n, q_1) & \cdots & \omega(p_n, q_n) \end{bmatrix} \in R^{n\times n} \tag{13}$$

Each element in the covariance matrix represents the covariance between the i-th coordinate of point set p and the i-th coordinate in point set q. Specifically, the diagonal elements $\sigma(p_i, q_i)$ indicate the correlation between the i-th dimension of p and the i-th dimension of q. A value close to 0 suggests no significant correlation, a positive value indicates a positive correlation, and a negative value implies a negative correlation.

Thus, the diagonal elements represent the variance of each dimension, providing insights into the data distribution and the extent of transformation. The off-diagonal elements of the covariance matrix represent the correlation between different dimensions. Analyzing the covariance matrix helps reveal linear relationships between dimensions can and the underlying data structure. Therefore, SVD is applied to extract key information from the covariance matrix.

Performing SVD on the covariance matrix yields the matrices U、Σ、V^T, which are used to determine the optimal rotation matrix R. For the rotation matrix, the least square's objective function is:

$$\mathrm{E}^2 = \sum_{i=1}^{N} (q_i - Rp_i)^T (q_i - Rp_i) \tag{14}$$

By simplifying the above equation, we obtain:

$$\mathrm{E}^2 = \sum_{i=1}^{N} (q_i^T q_i + p_i^T p_i - 2q_i^T R p_i) \tag{15}$$

Because the first two terms are constants, minimizing E^2 is equivalent to maximizing the last term. We define:

$$F = \sum_{i=1}^{N} q_i^T R p_i \tag{16}$$

The objective then becomes finding the rotation matrix R that maximizes F. Simplifying F gives:

$$F = \mathrm{Trace}\left(\sum_{i=1}^{N} R p_i q_i^T\right) = \mathrm{Trace}\left(R \sum_{i=1}^{N} p_i q_i^T\right) = \mathrm{Trace}(RH) \tag{17}$$

In the equation, $H = \sum_{i=1}^{N} p_i q_i^T$.

Let A be a symmetric positive-definite matrix. For any orthogonal matrix B, the following holds:

$$\mathrm{Trace}(A) \geq \mathrm{Trace}(BA) \tag{18}$$

Thus, to maximize F, it is sufficient to find the rotation matrix R such that RH is a symmetric positive-definite matrix. Given that $H=U\Sigma V^T$, let $R=VU^T$.

Substituting this into the expression for RH gives:

$$RH = (VU^{\mathrm{T}})(U\Sigma V^{\mathrm{T}}) = V\Sigma V^{\mathrm{T}} \tag{19}$$

At this point, RH is a symmetric positive-definite so $R=VU^T$ maximizes F.

Improvement of SVD-based spatial registration

As discussed in Introduction, three non-collinear points are sufficient to uniquely determine a rigid transformation, including both rotation and translation [15]. If fewer than three points are available, the transformation cannot be uniquely defined.

Conversely, using more than three points introduces redundancy, potentially leading to an over-constrained system. Since the goal is to minimize the registration error $\mathrm{E(R,T)}$, selecting

Table 1. Parameters of random transformations

Coordinate Axes	Euler Angles (°)	Translation (mm)
X Axis	42.59	9.96
Y Axis	40.53	7.72
Z Axis	-32.12	3.97

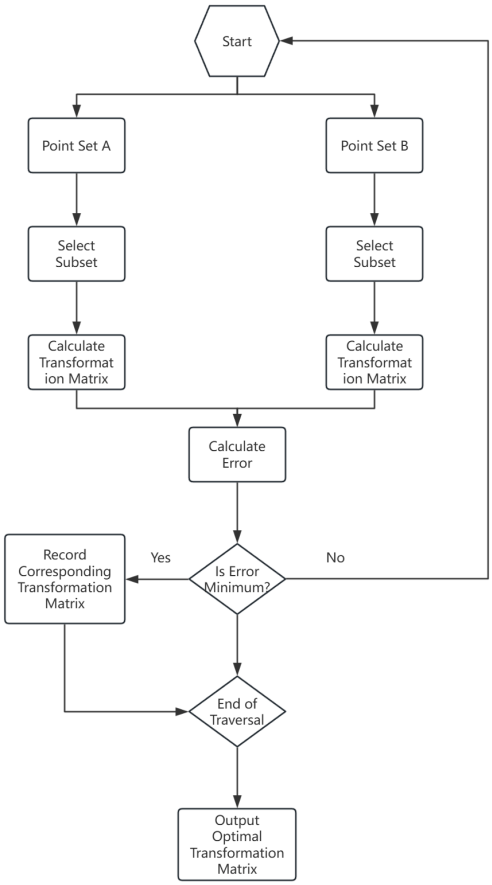

Figure 2. Flowchart of the improved SVD algorithm. SVD, singular value decomposition.

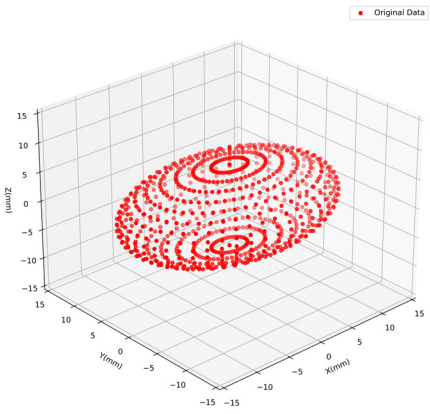

Figure 3. Three-dimensional virtual elliptical point cloud data.

three corresponding points is a practical choice to compute the transformation [16]. However, in real-world scenarios, visualization errors, noise, and electromagnetic interference may distort the point data. To reduce the influence of any single point on the transformation outcome, additional points are included in the point sets. Theoretically, with low noise levels, increasing the number of points improves the robustness and accuracy of the estimated transformation matrix [17].

In practice, however, the accuracy of the newly added points cannot be guaranteed. If points with significant errors are introduced, the overall transformation accuracy may deteriorate. To address this issue, we propose an improved spatial registration algorithm. This method iteratively selects subsets of three corresponding points from the full point set to compute candidate transformation matrices. Each matrix was applied to the original source point set to generate a transformed set, which was then compared to the target set. The transformation matrix yielding the smallest registration error was selected as the optimal solution. The overall workflow is illustrated in **Figure 2**.

Experiment and results analysis

Simulation experiment

A three-dimensional point set was first generated as the source dataset. Random rotation and translation transformations were then applied to this point set, with the corresponding parameters recorded as the ground truth. To simulate real-world conditions, random noise was added during the transformation process, producing a noisy target point set.

Both the standard SVD algorithm and the proposed improved algorithm were used to register the two-point sets. The resulting transformation matrices were used to extract Euler angles and translation vectors, which were compared against the ground truth to evaluate registration accuracy.

The synthetic point cloud was generated using scientific libraries such as NumPy and Pandas, forming a three-dimensional virtual elliptical distribution, as shown in **Figure 3**. A series of random transformations was then applied to obtain the target point cloud. The parameters of the random transformation are summarized in **Table 1**.

Table 2. Calculated random transformation parameters

Coordinate Axes	Original Transformation	SVD Algorithm	Improved Algorithm
X Axis	42.59	42.47	42.70
Y Axis	40.53	40.63	40.52
Z Axis	-32.12	-32.54	-32.38

Note: SVD, singular value decomposition.

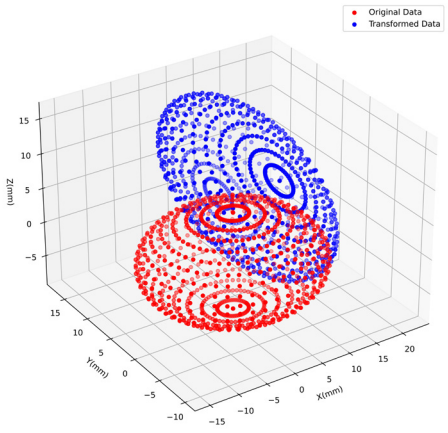

Figure 4. Comparison of point cloud data before and after transformation.

Rotation matrix and transformation matrix construction

The rotation matrix is derived from sequential rotations around the X-, Y-, and Z-axes, as defined by the following

$$\mathbf{R}_{xyz}(\alpha,\beta,\gamma) = \mathbf{R}_x(\alpha)\mathbf{R}_y(\beta)\mathbf{R}_z(\gamma) \tag{20}$$

In the formula,

$$\mathbf{R}_x(\alpha) = \begin{pmatrix} 1 & 0 & 0 & 0 \\ 0 & \cos\alpha & -\sin\alpha & 0 \\ 0 & \sin\alpha & \cos\alpha & 0 \\ 0 & 0 & 0 & 1 \end{pmatrix}$$

$$\mathbf{R}_y(\beta) = \begin{pmatrix} \cos\beta & 0 & \sin\beta & 0 \\ 0 & 1 & 0 & 0 \\ -\sin\beta & 0 & \cos\beta & 0 \\ 0 & 0 & 0 & 1 \end{pmatrix}$$

$$\mathbf{R}_z(\gamma) = \begin{pmatrix} \cos\gamma & -\sin\gamma & 0 & 0 \\ \sin\gamma & \cos\gamma & 0 & 0 \\ 0 & 0 & 1 & 0 \\ 0 & 0 & 0 & 1 \end{pmatrix}$$

The specific expression is given by:

$$\mathbf{R}_{xyz}(\alpha,\beta,\gamma) = \begin{bmatrix} \cos\alpha\cos\gamma - \cos\beta\sin\alpha\sin\gamma & -\cos\beta\cos\gamma\sin\alpha - \cos\alpha\sin\gamma & \sin\alpha\sin\beta \\ \cos\gamma\sin\alpha + \cos\alpha\cos\beta\sin\gamma & \cos\alpha\cos\beta\cos\gamma - \sin\alpha\sin\gamma & -\cos\alpha\sin\beta \\ \sin\beta\sin\gamma & \cos\gamma\sin\beta & \cos\beta \end{bmatrix} \tag{21}$$

Substituting the data, the rotation matrix is solved as:

$$\mathbf{R}_{xyz}(\alpha,\beta,\gamma) = \begin{bmatrix} 0.64372277 & 0.76390755 & 0.04545592 \\ -0.40408034 & 0.38974887 & -0.82753544 \\ -0.64987696 & 0.51433556 & 0.55957025 \end{bmatrix} \tag{22}$$

The translation vector is constructed based on the translation distances:

$$t = [9.9572333 \quad 7.72319645 \quad 3.97196656]^t \tag{23}$$

By combining the rotation matrix and the translation vector, the 4×4 transformation matrix T is formed:

$$T = \begin{bmatrix} R & t \\ 0 & 1 \end{bmatrix} \tag{24}$$

By substituting the data:

$$T = \begin{bmatrix} 0.64372277 & 0.76390755 & 0.04545592 & 9.9572333 \\ -0.40408034 & 0.38974887 & -0.827535440 & 7.72319645 \\ -0.64987696 & 0.51433556 & 0.55957025 & 3.97196656 \\ 0 & 0 & 0 & 1 \end{bmatrix} \tag{25}$$

Following established practices in registration and point cloud matching research, Gaussian noise was introduced during coordinate transformation to simulate real-world uncertainties, such as electromagnetic interference and sensor measurement errors [18-20]. Specifically, the transformation matrix was applied to the original point cloud data, and random noise was added during this process to mimic real-world conditions, generating a new set of point cloud data. This data is visualized in **Figure 4**, where blue points represent the new point cloud data.

Both the standard SVD algorithm and the improved version were applied to the original and noisy point clouds. Euler angles and translation vectors were computed from the resulting transformation matrices and compared with the ground truth parameters (**Table 2**).

The translation errors were minimal and are therefore omitted. Squared differences for each point set are shown in **Figure 5**.

As shown, both algorithms achieved high spatial transformation accuracy. However, in practical applications—such as surgeries involving

Table 3. Transformation parameters after adding high-error points

Coordinate Axes	Original Transformation	SVD Algorithm	Improved Algorithm
X Axis	42.59	39.97	42.82
Y Axis	40.53	43.64	40.03
Z Axis	-32.12	-34.17	-36.93

Note: SVD, singular value decomposition.

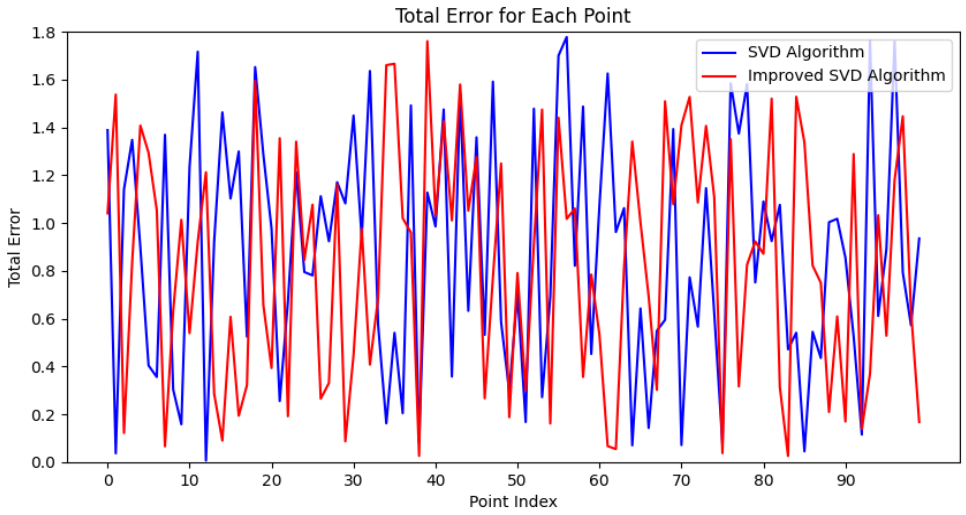

Figure 5. Squared differences for each point set.

electromagnetic tracking—metallic interference could introduce substantial error to individual data points. To simulate this, controlled perturbations were introduced into the dataset.

In such cases, traditional SVD cannot identify or exclude outliers, as it gives equal weight to all correspondences. Consequently, registration accuracy declines when outliers are present.

The improved algorithm addresses this limitation by iteratively selecting subsets of three corresponding points and identifying the transformation matrix that minimizes registration error. This approach effectively reduces the influence of erroneous data points.

The experiment is repeated with a small number of deliberately introduced high-error points. The performance of both algorithms is shown in the **Table 3**. The average squared differences for each method are shown in **Figure 6**.

The results clearly demonstrated that the conventional SVD algorithm is vulnerable to outliers. Because it incorporates all point correspondences—including those with large deviations—into its computation, it suffers from decreased registration accuracy.

In contrast, the improved SVD algorithm employed a robust outlier rejection mechanism prior to transformation estimation. By selectively retaining geometrically consistent point pairs through iterative consistency evaluation, the algorithm enhanced registration precision and minimizes the impact of noisy or erroneous data points.

Physical model experiment

In the physical model experiment, two coordinate systems were established: the electromagnetic coordinate system of external fiducial markers and their corresponding 3D coordinates in the medical image space. Specifically, electromagnetic sensors are affixed to the patient's skin as fiducial points. CT scanning was then performed to acquire medical images containing these markers. Simultaneously, the electromagnetic navigation system continuously tracked the pose of each fiducial point in real time.

First, the coordinates of the fiducial points in both systems were registered to derive a transformation matrix between the electromagnetic and medical image coordinate systems. Subsequently, an electromagnetic sensor was mounted on the surgical instrument. Using the transformation matrix, the instrument's position was displayed in the medical image coordinate space, thereby enabling real-time image-guided navigation to the target lesion.

Since the physical model lacks CT data, its dimensions and lesion coordinates were predefined. Based on the principles of im-

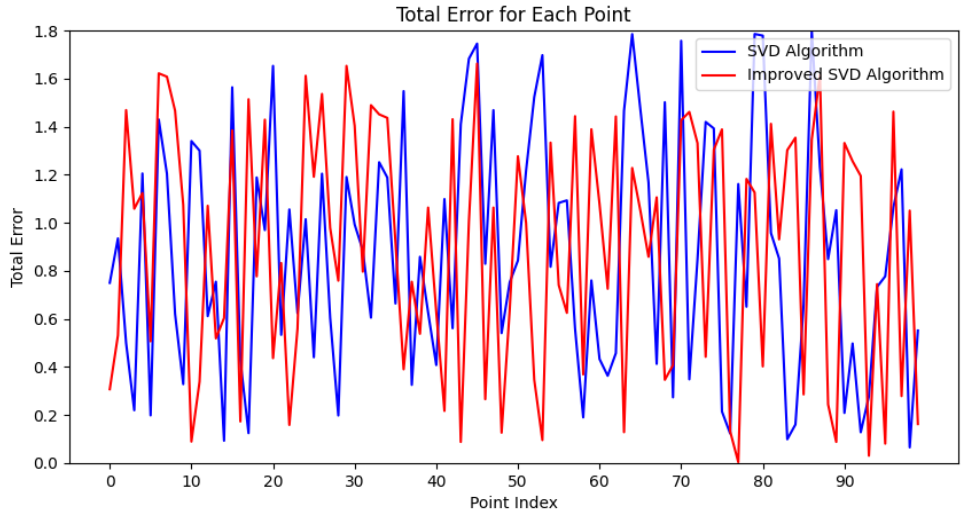

Figure 6. Squared differences after adding high-error points.

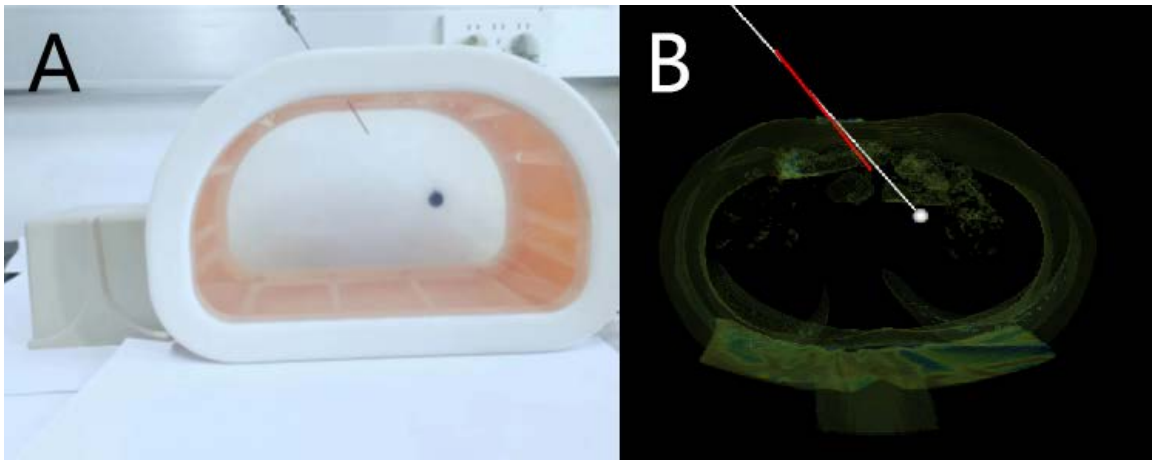

Figure 7. Navigation system integrated with physical model. (A) Navigation System Overview; (B) Integration with Phantom.

age-based coordinates, a virtual image space is constructed. Fiducial sensors were positioned at designated locations, and their coordinates in the virtual environment were obtained. Given the known location of the lesion in the physical model, its image-space coordinates can also be derived.

By aligning the electromagnetic and image coordinates, the system guided the ablation needle to the target, as illustrated in **Figure 7**. The white lines indicate the planned navigation path, and the red lines show the real-time position of the ablation needle.

An electromagnetic sensor was affixed to the tip of the ablation needle to capture its real-time pose. A local coordinate system was established with the sensor's center as the origin. Using the known geometry and mounting location of the ablation needle, the needle tip's position in the local coordinate system was calculated. This is then transformed into the electromagnetic coordinate system. Applying the precomputed transformation matrix, the needle tip's position was finally represented in the medical image space. Since the coordinates of the lesion are known, the needle tip can be precisely guided into the target under real-time image navigation.

To validate the feasibility of the proposed algorithm, a series of physical experiments were conducted. In the first experiment, six sensors were placed on a simulated tissue to mimic the location of potential model to emulate lesions. Guided by the navigation software interface, a biopsy needle was inserted into the model based on system instructions.

During the procedure, the clinician adjusted the needle in real time via the software interface, ensuring that the virtual needle and its tip aligned with the preplanned puncture path.

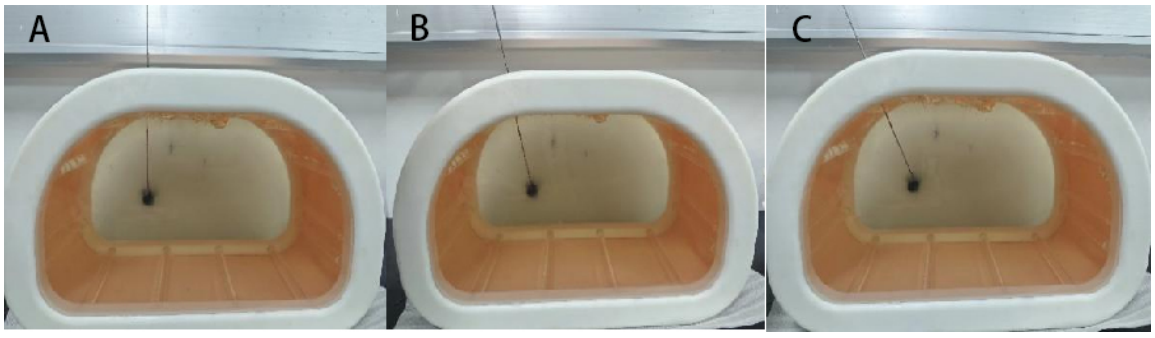

Figure 8. Needle insertion into simulated tissue. (A) Insertion at 0°; (B) Insertion at 5°; (C) Insertion at 10°.

Table 4. Root mean square error for needle insertions at different angles using the improved SVD algorithm

	0	5	10
Maximum Value	1.21	1.2	0.98
Standard Deviation	1.01	1.03	0.73

Note: SVD, singular value decomposition.

Table 5. Root mean square error for needle insertions at different angles using the traditional SVD algorithm

	0	5	10
Maximum Value	1.38	1.25	1.19
Standard Deviation	1.22	1.19	0.84

Note: SVD, singular value decomposition.

As shown in **Figure 8**, needle insertions were performed at three angles: 0°, 5°, and 10°. To minimize electromagnetic interference, all potential sources were kept at least 2 meters away from the setup (FG ≤ 2 m).

First, a target point was defined within the simulated tissue. The navigation system was used to identify its coordinates, and the relative positioning between the needle tip and the target was calculated. The path was then planned and executed accordingly. Once the needle tip reached the target, its final position was recorded using the navigation system. These data were used to evaluate localization accuracy. All participating clinicians had prior experience operating the navigation system.

To assess the precision of the experiment, the standard deviation of multiple insertions was calculated:

$$SD = \sqrt{\frac{1}{n-1}\sum_{i=1}^{n} |p_i p|^2} \tag{26}$$

In the formula, p_i represents the needle tip position in the i-th insertion, and the centroid position of the point cloud formed by the needle tip's position in the n-th insertion.

In this experiment, the accuracy was validated by measuring the root mean square error between the actual needle tip positions and the target lesion location. The formula is as follows:

$$RMSE = \sqrt{\frac{\sum_{i=1}^{n} | p_{\text{obs},i} p_{\text{tru},i} |^2}{n}} \tag{27}$$

In the formula, $p_{\text{obs},i}$ represents the actual needle tip position in the i-th insertion, and ptru, $p_{\text{tru},i}$ denotes the target lesion position for the i-th insertion.

The experimental results are presented in **Table 4**. Each needle insertion angle (0°, 5°, and 10°) was tested 100 times. For every five insertions, the centroid of the resulting point cloud was calculated, and its root mean square error relative to the target lesion location was computed.

Similarly, using the traditional SVD algorithm, needle insertions at angles of 0°, 5°, and 10° were repeated 100 times into the same lesion. The centroid of the point cloud formed by the actual needle tip positions from every five insertions was calculated. The root mean square error between each centroid and the target lesion position was then computed (**Table 5**).

The comparison results indicate that the improved SVD algorithm consistently achieved lower maximum errors and smaller standard deviations across all insertion angles. These

findings highlight the enhanced accuracy and stability of the improved algorithm compared to the traditional approach.

Notably, at angles of 10° and 15°, the reductions in both maximum error and variability were particularly substantial, suggesting that the improved algorithm can more effectively limit deviation in needle trajectory. In clinical scenarios, this capability translates into more accurate targeting of the lesion, improved surgical success rates, and enhanced postoperative recovery for patients.

Conclusion

In conclusion, the improved SVD algorithm demonstrates not only theoretical advantages but also excellent performance in practical applications. By minimizing registration errors caused by variations in needle insertion angles, the algorithm significantly improves the precision and safety of tumor ablation procedures. Its high clinical applicability and potential for widespread implementation are evident.

Future work should focus on further optimizing the algorithm by incorporating diverse clinical datasets and applying it to various tumor types, thereby strengthening its robustness and broadening its scope of application in interventional oncology.

Author contributions: This study was conceived and co-designed by Xinyao Li and Gaoshuai Chen. Xinyao Li, as the project leader and corresponding author, was responsible for determining the research protocol, supervising project progress, acquiring funding, writing the original draft, and reviewing and finalizing the manuscript. Gaoshuai Chen contributed to the development of the core research ideas and was primarily responsible for developing analytical tools, data analysis, and results visualization. Xin Yang provided key contributions in terms of theoretical guidance and in-depth analysis of the results. Yuchao Liu was responsible for data collection, curation, and validation. Yu Xia provided experimental resources, technical support for the research, and contributed to discussion of findings. All authors have read and approved the final manuscript.

References

[1] Hering A, Hansen L, Mok TCW, et al. Learn2Reg: Comprehensive Multi-Task Medical Image Registration Challenge, Dataset and Evaluation in the Era of Deep Learning. IEEE Trans Med Imaging 2023;42(3):697-712.

[2] Takai H, Murayama M, Kii S, et al. Accuracy analysis of computer-assisted surgery for femoral trochanteric fracture using a fluoroscopic navigation system: Stryker ADAPT® system. Injury 2018;49(6):1149-1154.

[3] Takeba J, Umakoshi K, Kikuchi S, et al. Accuracy of screw fixation using the O-arm® and StealthStation® navigation system for unstable pelvic ring fractures. Eur J Orthop Surg Traumatol 2018;28(3):431-438.

[4] Jackson P, Simon R, Linte C. Surgical Tracking, Registration, and Navigation Characterization for Image-guided Renal Interventions. Annu Int Conf IEEE Eng Med Biol Soc 2020;2020:5081-5084.

[5] Sun M, Rao L, Zhang C, et al. Analysis of influence of surgical instruments on accuracy of magnetic navigation system for craniofacial surgery robots. Comput Assist Surg (Abingdon) 2023;28(1):2210744.

[6] Li J, Deng Z, Shen N, et al. A fully automatic surgical registration method for percutaneous abdominal puncture surgical navigation. Comput Biol Med 2021;136:104663.

[7] Wagner A, Schicho K, Birkfellner W, et al. Quantitative analysis of factors affecting intraoperative precision and stability of optoelectronic and electromagnetic tracking systems. Med Phys 2002;29(5):905-912.

[8] Stevens F, Conditt MA, Kulkarni N, et al. Minimizing electromagnetic interference from surgical instruments on electromagnetic surgical navigation. Clin Orthop Relat Res 2010;468(8):2244-2250.

[9] Lian C, Li X, Kong L, et al. CoCycleReg: Collaborative cycle-consistency method for multi-modal medical image registration. Neurocomputing 2022;500:799-808.

[10] Zhou Z, Yang Z, Jiang S, et al. Augmented reality surgical navigation system based on the spatial drift compensation method for glioma resection surgery. Med Phys 2022;49(6):3963-3979.

[11] Xiong F, Kong Y, Xie S, et al. Spatial deformable transformer for 3D point cloud registration. Sci Rep 2024;14(1):5560.

[12] Agostinho S, Ošep A, Bue AD, et al. (Just) A Spoonful of Refinements Helps the Registration Error Go Down. 2021 IEEE/CVF International Conference on Computer Vision (ICCV) 2021;6088-6097.

[13] Li Z, Wang C, Ma J, et al. Point set registration via rigid transformation consensus. Comput Electr Eng 2022;101:108098.

[14] Chatrasingh M, Wiratkapun C, Suthakorn J. A generalized closed-form solution for 3D registration of two-point sets under isotropic and anisotropic scaling. Results Phys

2023;51:106746.

[15] Horn B. Closed-form solution of absolute orientation using unit quaternions. J Opt Soc Am A 1987;4:629-642.

[16] Wang GH, Liu T, Tang ZW, et al. Model assembly error analysis method based on local feature registration. Aeronaut Manuf Technol 2021;(03):33-6+41.

[17] Huang X, Mei G, Zhang J. Feature-Metric Registration: A Fast Semi-Supervised Approach for Robust Point Cloud Registration Without Correspondences. 2020 IEEE/CVF Conference on Computer Vision and Pattern Recognition (CVPR) 2020;11363-11371.

[18] Ma JY, Zhao J, Tian JW, et al. Robust point matching via vector field consensus. IEEE Trans Image Process 2014;23(4):1706-1721.

[19] Charles RQ, Su H, Kaichun M, et al. PointNet: Deep Learning on Point Sets for 3D Classification and Segmentation. 2017 IEEE Conference on Computer Vision and Pattern Recognition (CVPR) 2017;77-85.

[20] Besl PJ, McKay ND. A method for registration of 3-D shapes. IEEE Trans Pattern Anal Mach Intell 1992;14(2):239-256.